Energy spectra of atmospheric muons measured with the CAPRICE98 balloon experiment

M. Boezio, V. Bonvicini, P. Schiavon, A. Vacchi, and N. Zampa
University of Trieste and Sezione INFN di Trieste, Via A. Valerio 2, I-34147 Trieste, Italy

D. Bergström, P. Carlson, T. Francke, P. Hansen, and E. Mocchiutti
Royal Institute of Technology (KTH), AlbaNova University Center (SCFAB), S-10691 Stockholm, Sweden

M. Suffert
Centre des Recherches Nucléaires, BP20, F-67037 Strasbourg Cedex, France

M. Hof, J. Kremer, W. Menn, and M. Simon
Universität Siegen, 57068 Siegen, Germany

M. Ambriola, R. Bellotti, F. Cafagna, F. Ciacio, M. Circella, and C. N. De Marzo
University of Bari and Sezione INFN di Bari, Via Amendola 173, I-70126 Bari, Italy

P. Papini, S. Piccardi, P. Spillantini, and E. Vannuccini
University of Firenze and Sezione INFN di Firenze, Largo E. Fermi 2, I-50125 Firenze, Italy

S. Bartalucci and M. Ricci
INFN–Laboratori Nazionali di Frascati, Via E. Fermi 40, CP 13, I-00044 Frascati, Italy

M. Casolino, M. P. De Pascale, A. Morselli, P. Picozza, and R. Sparvoli
University of Roma "Tor Vergata" and Sezione INFN di Roma II, Via della Ricerca Scientifica 1, I-00133 Roma, Italy

J. W. Mitchell, J. F. Ormes, S. A. Stephens, and R. E. Streitmatter
Code 661, NASA/Goddard Space Flight Center, Greenbelt, Maryland 20771

U. Bravar and S. J. Stochaj
R. L. Golden Particle Astrophysics Lab, Box 3 PAL, New Mexico State University, Las Cruces, New Mexico 88003

(Received 14 February 2003; published 24 April 2003)

The measurement of the atmospheric muon spectrum is currently of great interest because of the study of atmospheric neutrinos and the claim of neutrino oscillations made in 1998 by the Super-Kamiokande Collaboration. A measurement of the muon flux is an indirect measure of the neutrino flux. Therefore, it can be used to improve the calculation of the atmospheric neutrino flux, which in turn can be compared with the observed neutrino rates in underground detectors. This article reports a new measurement of the μ^+ and μ^- spectra at several atmospheric depths in the momentum ranges 0.3–20 GeV/c and 0.3–40 GeV/c, respectively. The data were collected by the balloon-borne experiment CAPRICE98 during the ascent of the payload on 28 May 1998 from Fort Sumner, N. M. The experiment used the NMSU-WIZARD/CAPRICE 98 balloon-borne magnet spectrometer equipped with a gas ring imaging Cherenkov detector and a silicon-tungsten calorimeter.

DOI: 10.1103/PhysRevD.67.072003 PACS number(s): 96.40.Tv, 14.60.Ef, 14.60.Pq

I. INTRODUCTION

The energy spectrum of atmospheric muons is currently of great interest because of the potential to cross-check the results from simulations of the propagation of cosmic rays in the atmosphere. In these simulations, the correlation between the muon flux and the neutrino flux is of particular importance. The recent detailed studies of atmospheric neutrino interactions by the Super-Kamiokande [1], Soudan-2 [2], and MACRO Collaborations [3] give strong support for neutrino oscillations. These results, however, are not based on comparisons with the absolute flux. The parameters of oscillations depend on the absolute production spectrum of neutrinos which can be checked by measuring the atmospheric muon flux. The majority of the Super-Kamiokande events, the "sub-GeV" events, have neutrino energies typically below 1 GeV, corresponding to typical muon momenta of about 3 GeV/c. At Super-Kamiokande, where the geomagnetic cutoff is about 12 GV rigidity, these neutrinos are generated, on the average, by incident protons of energy of about 10–20 GeV [4]. In addition to the importance of muon flux measurements for the neutrino oscillation results, a test of the simulation at these energies provides the degree of confidence such simulations can have at much higher energies [5]. Experiments such as the Akeno Giant Air Shower Array (AGASA), HiRes, and Auger use air shower simulation programs to calculate secondary atmospheric particle fluxes (e.g., see [6]).

There are three major factors that are of special impor-

tance for the calculation of the neutrino flux: (1) the incident cosmic-ray flux, (2) the hadronic production model, and (3) geomagnetic and solar modulation effects. In 1996, Gaisser *et al.* [7] compared different calculations of the atmospheric neutrino flux and concluded that there are differences at the level of 30%. In a more recent study Gaisser and Honda [8] and, separately, Gaisser [4], conclude that the estimated neutrino flux for the Super-Kamiokande experiment, using the same hadronic model (code *Target 2.1*), varies by about 10% for different measured incident cosmic-ray spectra. For a detailed discussion of the incident cosmic-ray flux, the reader may refer to the recent CAPRICE98 results [9] and it may be mentioned that below 10 GV the incident flux is affected by the periodic solar activity and the geomagnetic field. The same authors [4,8] also compared the neutrino flux using different hadronic interaction models. Here the differences in the neutrino flux around 1 GV are larger, about 20%. Accelerator data on the yield of pions from proton-nuclei interactions do not cover the full phase space. Results from different experiments, many performed in the 1960s or 1970s, are often not consistent. However, a recent experiment at CERN, HARP [10], measures, in a systematic way, the particle production over almost the full phase and should be able to substantially improve the situation. In addition to the uncertainties in the flux, most simulations use a one-dimensional approach in which the secondaries are assumed to be collinear with the incident cosmic-ray particle (for a discussion of the effects of this approximation, see [4]).

The flux of muons in the atmosphere increases with atmospheric depth, reaches a maximum around an altitude corresponding to atmospheric depths of 100–200 g/cm^2 (e.g., see [11]), and then decreases with depth. The location of the maximum and the rate of decrease depend weakly on the energy. Muon measurements should therefore be performed over a broad range of altitudes and energies. In the last decade a few measurements of atmospheric muons were performed by various groups [12–15]. Recently, we have also presented muon flux measurements obtained with the CAPRICE94 instrument [11], capable of measuring μ^+ in the momentum range 0.3–2 GeV/c and μ^- in the range 0.3–40 GeV/c. In this paper we present new results on atmospheric muon fluxes obtained with the CAPRICE98 instrument. This modified spectrometer allowed measurements of μ^+ and μ^-, both over large ranges of 0.3–20 GeV/c and 0.3–40 GeV/c, respectively. The CAPRICE98 instrument also measured the cosmic-ray hydrogen and helium spectra [9] and these can be used as input for shower simulations in order to reduce the overall systematic uncertainties associated directly with the spectrometer. Data on the muon flux at the ground were collected in 1997 with the present spectrometer and have been published [16].

In this paper, the detector system of the CAPRICE98 experiment is described in Sec. II, the data analysis is in Secs. III and IV, and the results are given in Sec. V.

II. THE EXPERIMENT

The CAPRICE98 spectrometer was flown by balloon from Ft. Sumner, N. M., (34.28° north latitude, 104.14° west longitude), on 28 May 1998 [17]. After three hours of balloon ascent, the payload reached an altitude of 36 km. It floated for more than 20 h between altitudes from 36 to 38 km corresponding to an average residual atmospheric depth of 5.5 g/cm^2. At this float altitude, the spectrometer collected data on the flux of various cosmic particles: antiprotons, electrons, positrons, hydrogen, deuterium and helium nuclei; most of these results have been published [9,18–20]. The instrument, shown in Fig. 1, consisted, from top to bottom, of a ring imaging Cherenkov (RICH) detector, a time-of-flight (TOF) system, a superconducting magnet spectrometer equipped with drift chambers (DCs), and a silicon-tungsten imaging calorimeter. The major change in this instrument from that of CAPRICE94 is the replacement of the solid RICH detector [21], which had a threshold Lorentz factor $\gamma_L = 1.5$, by a gas RICH detector with a much higher threshold of $\gamma_L \approx 19$.

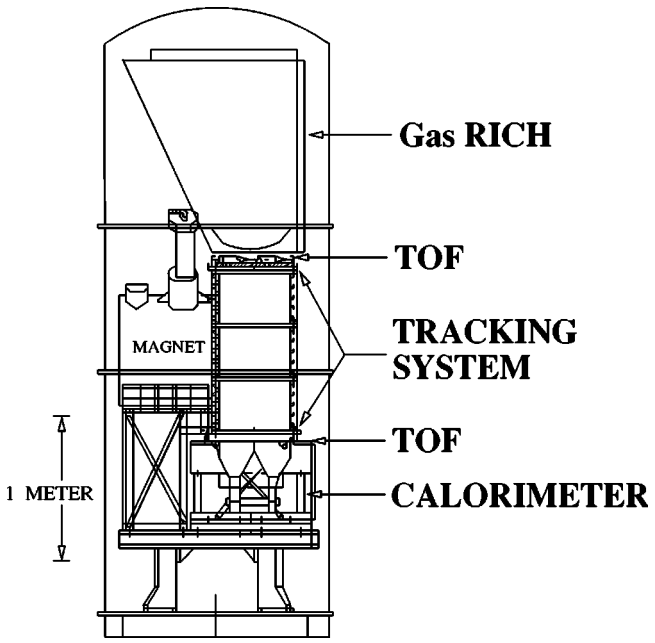

FIG. 1. A schematic view of the CAPRICE98 detector.

We give here a few details of the new RICH detector and briefly summarize the rest of the detectors of the instrument; the reader may refer to the earlier publications [17,22–27].

A. The gas RICH detector

The RICH detector [22–24] consisted of a 1 m tall gas radiator, filled with high purity C_4F_{10} gas. The detector threshold at float was $\gamma_L = 18.8$, corresponding to a threshold for muons of about 2 GeV/c and for protons of about 18 GeV/c. During the ascent of the balloon, the pressure of the gas was slightly different, giving an average threshold of $\gamma_L = 19.3$. The Cherenkov light produced in the gas was reflected by a spherical mirror, located at the bottom of the vessel, onto a multiwire proportional chamber (MWPC) filled with ethane to which was added the photosensitive agent TMAE (tetrakis-dimethyl-amino-ethylene) [23]. The photoelectron signals from the multiwire chamber were collected by 8×8 mm^2 pads in the 51×51 cm^2 pad plane. An

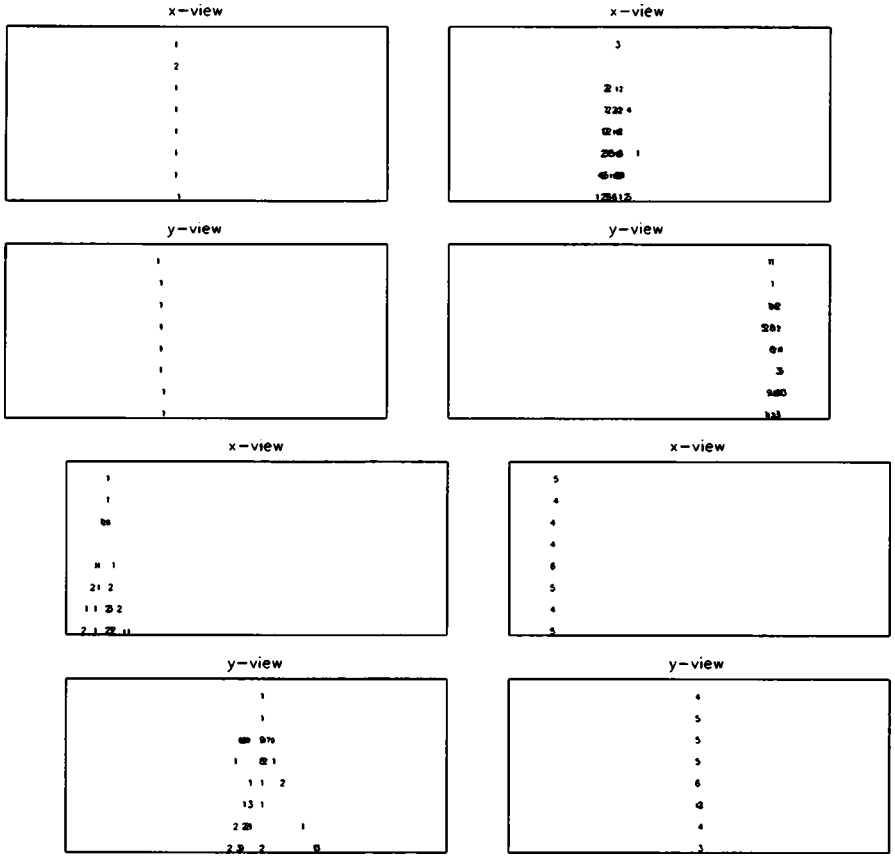

FIG. 2. Four different views of signals in the *x* and *y* planes of the calorimeter for different particles. The upper left view shows the track from a minimum ionizing particle. The numbers correspond to the signal size in each strip in mip. The upper right view shows an electromagnetic shower. The lower left view shows a hadronic interaction. The lower right view shows a noninteracting helium nucleus. Note that the figure is not to scale; the calorimeter is significantly thinner than shown in the figure.

extreme relativistic $Z=1$ particle with $\gamma>50$ emitted Cherenkov light at an angle of about 52 mrad and gave an average of 12 photoelectrons. The Cherenkov angle was calculated for each event from the hits in the pad plane using a Gaussian potential method [24]. The error in the angle determination was 1.2 mrad and the Cherenkov ring had a diameter of 11 cm for $\beta\simeq 1$ particles. The delicate RICH detector performed very well and made excellent particle identification. It was also used for the first time to cross-check the rigidity determination from the magnet spectrometer [9].

B. The time-of-flight system

The time-of-flight system was used to make a trigger, to determine the particle velocity from the time of flight, and its energy loss (dE/dx) in the scintillators. This system eliminated all upward-going particles, selected charge 1 particles (for the muon analysis), and was used for particle identification at lower momenta. The TOF resolution was about 230 ps.

C. The tracking system

The magnet spectrometer was equipped with a single-coil superconducting magnet [25], giving an inhomogeneous field and three sets of drift chambers [26]. These chambers provided 18 position measurements in the direction of maximum bending and 12 along the perpendicular direction. Particle rigidities were determined using the knowledge of the bending of the track and the field along the track. The maximal detectable rigidity was 300 GV.

D. The calorimeter

The calorimeter [27] had a sensitive area of 48×48 cm^2 and a total thickness of 7.2 radiation lengths, which corresponds to 0.33 nuclear interaction lengths. It provided topological information on both the longitudinal and lateral profiles of the charged particle interaction as well as the energy deposition. The calorimeter was used in the particle identification.

It is important to point out that the combination of three independent particle identification detectors, the TOF, the RICH, and the calorimeter, made it possible to reliably determine the selection and rejection efficiency of each of them. We show in Fig. 2 calorimeter views for four different kinds of particles in the *x* and *y* planes of the calorimeter. The rectangular frames show the boundaries of the calorimeter box. The numbers in the figure correspond to the signal detected in each strips in mip (the most probable energy loss by a minimum ionizing particle). Normally, a single particle deposits its energy in only one strip per plane. The upper left view of Fig. 2 shows a display of the signal from a minimum ionizing particle. This event was a muon with a measured rigidity of 6.2 GV. The upper right view shows a typical electromagnetic shower from a 1.6 GV positron. The lower left view shows a hadronic shower in the calorimeter, produced by a 5.0 GV proton. Note that the hadronic shower shows a much larger lateral spread than the electromagnetic shower. The lower right view shows a helium nucleus of rigidity of 32.5 GV traversing the calorimeter without interaction. Note that the signal in each strip was about four times

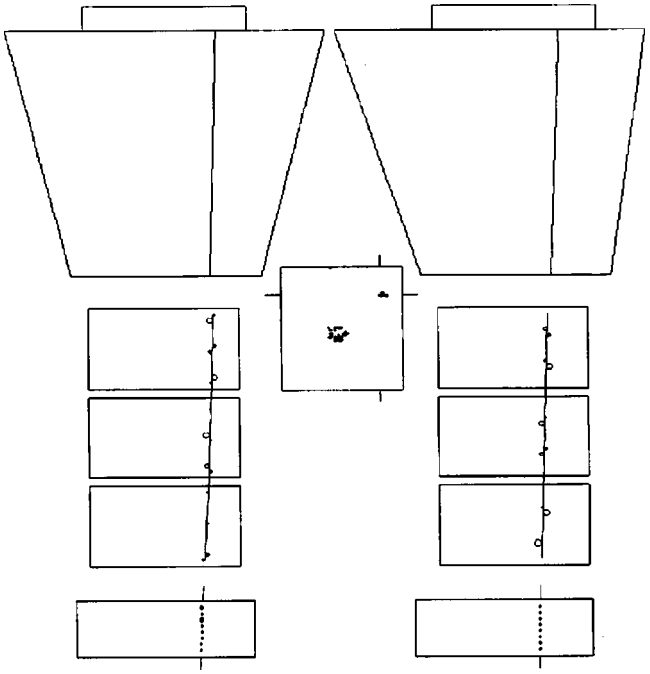

FIG. 3. A muon with a rigidity of 2.36 GV. It has the signature of a minimum ionizing particle going through the calorimeter. Note that the ionization signal in the upper right corner is well separated from the ring in the center produced by the Cherenkov light.

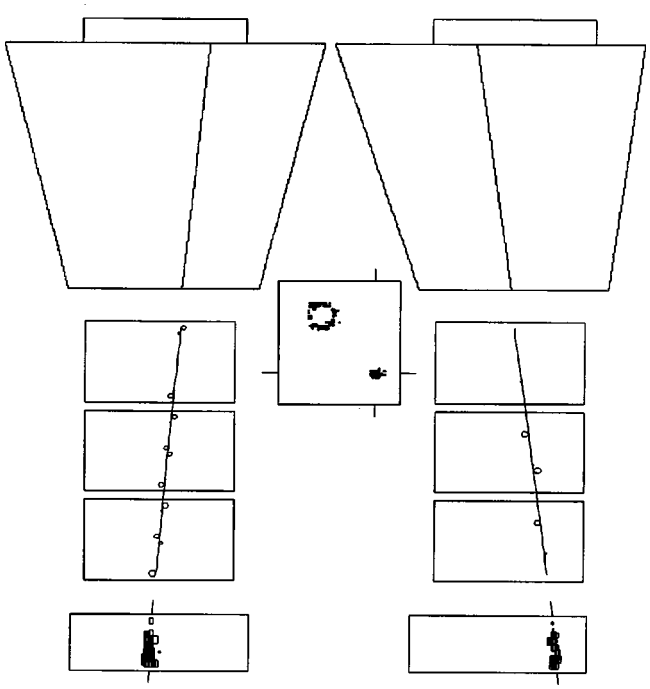

FIG. 4. An electron with a rigidity of 3.73 GV showing a clear signature of an electromagnetic shower in the calorimeter with a large Cherenkov ring.

larger than that produced by a minimum ionizing particle (upper left event), due to the large ionization loss for the doubly charged particle.

Figure 3 shows a 2.36 GV muon, producing a ring of pad hits by the Cherenkov light emitted by it in the multiwire proportional chamber. The typical signals for a minimum ionizing particle going through the calorimeter are clearly seen. Finally, Fig. 4 shows an electron of 3.73 GV with a similar pad-hit pattern in the RICH detector, but with an electromagnetic shower clearly visible in the calorimeter. This event shows a large ring of pad hits from the Cherenkov light in the multiwire proportional chamber because it is highly relativistic.

III. DATA ANALYSIS

A. Particle selection

The CAPRICE98 instrument was well suited to measure the muon spectra and charge ratio in the atmosphere against a background of electrons, protons, and heavier nuclei. The background for muon selection depends strongly on the atmospheric depth. At float the dominant background for positive muons is protons. With increasing atmospheric depth, the abundance of the proton component decreases, becoming a few percent of the positive muon component at ground level. The spectrometer accepted particles with a zenith angle less than 20° around the vertical, and the average zenith angle was about 9°. The particle identification was based on the determination of its rigidity by the spectrometer, velocity, either by the TOF detector at low energies or by the RICH detector at high energies, and the properties of energy deposit and topology in the calorimeter.

1. Tracking

To achieve a reliable estimation of the rigidity, the following two conditions were imposed on the fitted tracks: At least 10 (out of the 18) position measurements in the x direction and 6 (out of the 12) in the y direction were needed for the fit. There should be an acceptable chi squared value for the fitted track in both directions with stronger requirements on the x direction [9].

2. Scintillators and time-of-flight detector

The ionization loss dE/dx in the TOF scintillators was used to select minimum ionizing singly charged particles by requiring a measured dE/dx of less than 1.8 mip. From the TOF information, the particle velocity (β) was estimated. Downward-moving particles were selected by requiring $\beta > 0$, thereby eliminating contamination of albedo particles that remained in the selected sample. The velocity of the particle from the TOF detector was compared with that obtained from the fitted deflection assuming that the particle had the mass of a muon. An event was accepted as a muon if it had a β greater than the β obtained from the fitted deflection minus one standard deviation of the resolution (see Fig. 5).

Several conditions were also checked in order to point out possible errors in the signals. These errors were due to temperature variation and connected to time walk corrections, loading the calibration coefficients, mismatch between tracking and scintillation information, trigger coincidence failure, and so on. Events failing any of these conditions were removed from the analysis and properly accounted for in the efficiency study.

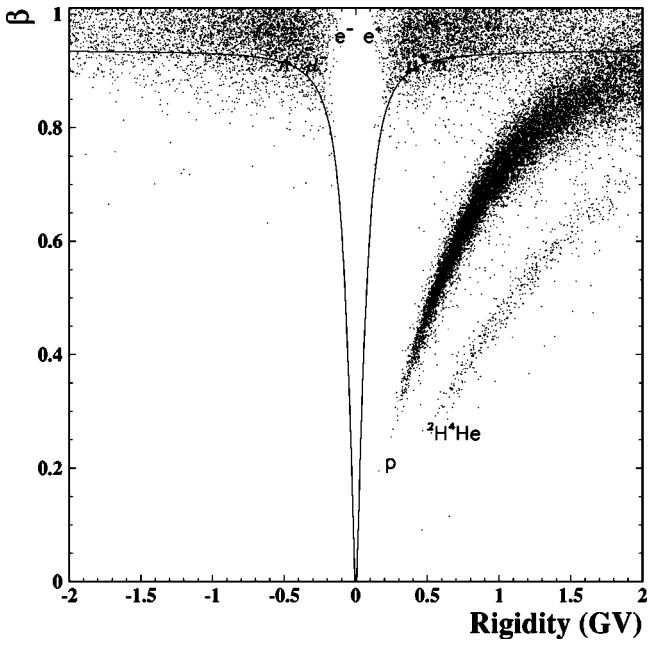

FIG. 5. The distribution of β from the time-of-flight information as a function of rigidity for ascent data. Events above the solid line were accepted as muons. The distributions corresponding to the various particles are labeled according to the particle species. The figure contains 23614 events.

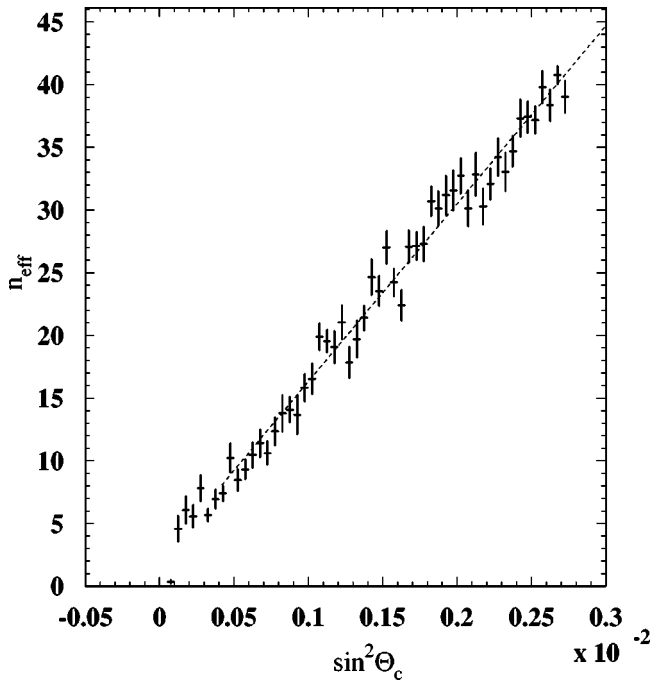

FIG. 6. Effective number of pads used in the Cherenkov angle fit for muons as a function of $\sin^2\theta_c$. The straight line is the fit to the data.

3. The RICH detector

The RICH detector was used to measure the Cherenkov angle of the particle and thereby its velocity. The Cherenkov angle was reconstructed from the geometrical distribution of the signals in the pad plane. The quality of the reconstruction depended on the number of pads used in the fit. Therefore, in order to have a reliable Cherenkov angle reconstruction, we used a condition based on the effective number of pads hit in the pad plane (n_{eff}) given by

$$n_{eff}=\frac{\left(\sum_i^{n_{pads}} \omega_i\right)^2}{\sum_i^{n_{pads}} \omega_i^2},$$

where ω_i is the weight of the Cherenkov angle of the pad i (see [23]).

n_{eff} is related to (but not the same as) the number of pads hit due to Cherenkov light and therefore to the number of photoelectrons (N_{ph}), which is related to the Cherenkov angle (θ_c) through

$$N_{ph}=N_0 L Z^2 \sin^2\theta_c = a \sin^2\theta_c, \tag{1}$$

where N_0 is the detector response parameter, L is the particle path length in the gas, in which it emits the Cherenkov light, and Z is the particle charge. Figure 6 shows n_{eff} as a function of $\sin^2\theta_c$. As expected, the data points follow a linear dependence and the gradient (A) has the value $A=13536 \pm 315$.

Then, by making use of the value of A in Eq. (1) we defined the following function $f(R)$ that varied with rigidity from a minimum of 5 to a maximum of 20:

$$g(R)=A \sin^2\theta_c - 5,$$

$$f(R)=\begin{cases} 20 & \text{if } g(R)>20, \\ g(R) & \text{if } 5<g(R)\leqslant 20, \\ 5 & \text{if } g(R)\leqslant 5. \end{cases}$$

Therefore, in the muon selection we required that the number of pads hit by the Cherenkov light should be greater than the value obtained from the function evaluated at a rigidity determined by the spectrometer. Figure 7 shows the variation of f with the rigidity.

Figure 8 shows the measured Cherenkov angle for 5843 particles in the momentum region up to 60 GeV/c. These particles passed the selection criteria for both the track and Cherenkov angle reconstruction. Muons started to produce Cherenkov photons in the C_4F_{10} gas at about 2 GeV/c and protons at about 18 GeV/c while electrons were above threshold in the entire momentum range of interest. Hence, below about 2 GeV/c, muons were selected requiring no light, while above this momentum they were selected according to their reconstructed Cherenkov angle. To accept a particle as a muon it was required that the measured Cherenkov angle agreed within three standard deviations of the resolution from the expected Cherenkov angle for the muon. Figure 8 also shows that for momenta higher than 50 GeV/c it was not possible to separate muons from protons because the Cherenkov angles did not differ by three standard deviations or more of the resolution. One can see that most of the elec-

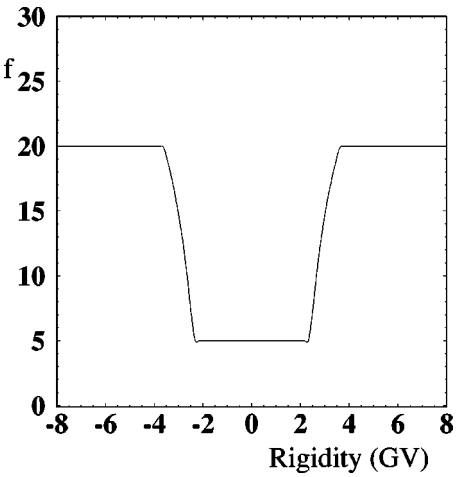

FIG. 7. Function $f(R)$ used in the muon selection to assure a reliable Cherenkov angle reconstruction.

trons and positrons are located at low energies (below 10 GV) and at maximum Cherenkov angle (about 52 mrad).

Since the resolution of the Cherenkov angle changes with rigidity, the difference between measured and calculated values for the Cherenkov angle (assuming a muon) for each rigidity bin was fitted with a Gaussian. The results are shown in Fig. 9.

The RICH detector was also used to reject events with multiple particles. Since particle ionization produced significantly higher signals than from the conversion of Cherenkov photons, we required that an event contained only one cluster

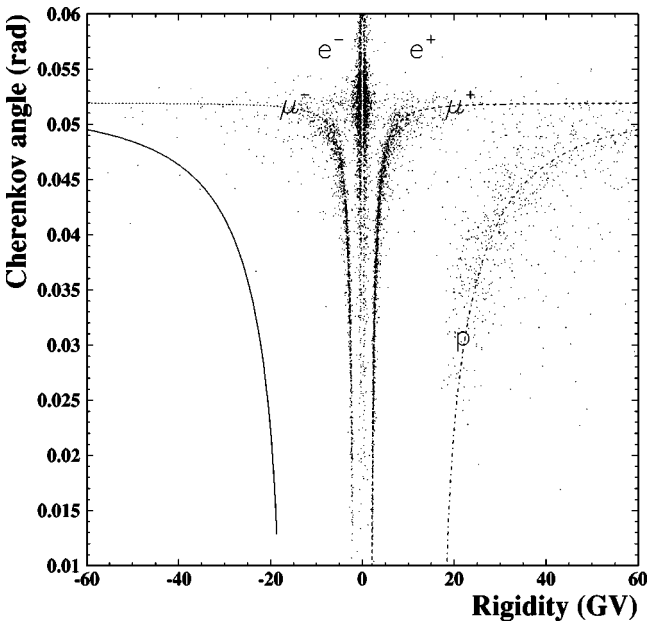

FIG. 8. Cherenkov angle for 5843 particles, measured by the CAPRICE98 experiment during ascent, as a function of rigidity. The events were singly charged particles chosen with a good reconstruction of the track and Cherenkov angle. The lines represent the theoretical values of the Cherenkov angle for muons, protons, and antiprotons. Most of the electrons and positrons were located at low energies (below 10 GeV) and at maximum Cherenkov angle.

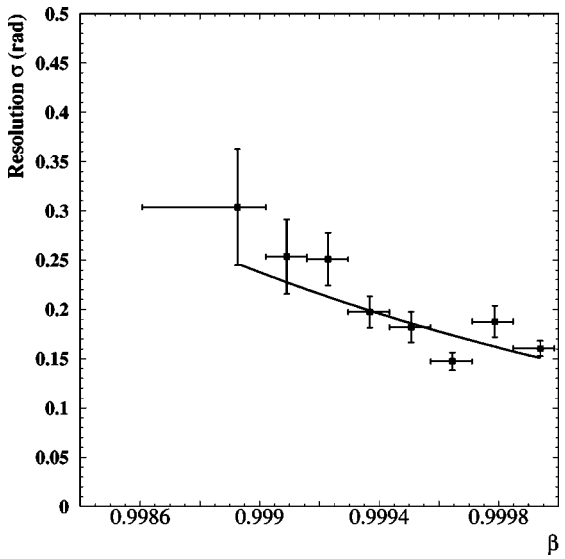

FIG. 9. The measured Cherenkov angle resolution as a function of the measured velocity (β) from ascent muon data. The line corresponds to the parametrization used in the analysis.

of pads with such a high signal. We also compared the position obtained from this signal with the one obtained from the tracking system in order to make sure that the signal obtained in the pad plane corresponded to the particle passing through the tracking system. It was found that at lower rigidity there was a larger disagreement between the two values, because lower energy particles scatter easily in the detector. Therefore, a response function was constructed using the data with rigidity as a variable, and a particle was accepted if the difference between the particle position in the pad and that extrapolated from the spectrometer was less than the value obtained from this response function. This last condition was not used with ground data because of the much smaller contamination of multiple charged particle events.

An important feature of the CAPRICE98 experiment is the ability to use the gas RICH detector to reject pions and estimate the background from them. Figure 10 shows the Cherenkov angle as function of deflection. The reconstructed Cherenkov angle was required to be more than 3 mrad (about 1 standard deviation for pions below 5 GeV/c) away from the expected Cherenkov angle for pions. This was done for momenta smaller than 5 GeV/c because at higher rigidities the difference between the Cherenkov angle for muons and pions is too small.

4. The calorimeter

The silicon-tungsten calorimeter used in the CAPRICE balloon flights was designed to identify particles by their energy deposits and topological properties.

The calorimeter was used in particle selection for momenta greater than 0.53 GeV/c. For lower momenta the electron shower was too small to be efficiently distinguished from a muon. The calorimeter selection was done using a variable n_{core}:

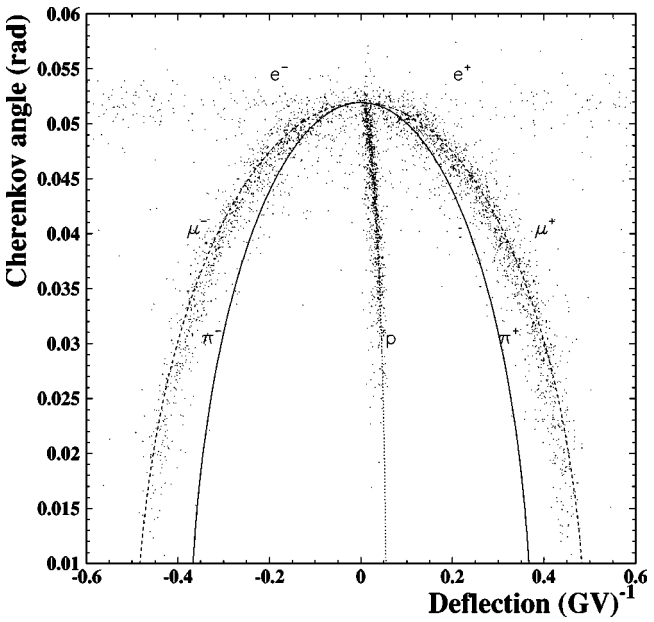

FIG. 10. Measured Cherenkov angle in the RICH detector as a function of deflection for a sample of particles collected during the ascent of the flight. The number of events in this plot is 3879. The lines represent the theoretical values of the Cherenkov angle for muons, protons, and pions.

$$n_{core} = \sum_{j=1}^{2} \sum_{i=1}^{8} n_{hit}(i,j)i,$$

where $n_{hit}(i,j)$ is the number of strips hit inside a cylinder of three Molière radii around the track in the ith plane (1 for the top plane and 8 for the bottom plane) of the jth view. This quantity strongly emphasises the multiplication of the secondaries with increased calorimeter depth. A minimum ionizing particle gives on the average a value of $n_{core}=72$, and hence a muon was defined as a particle with $n_{core}<80$.

A measurement of the ionization loss can be used to identify a particle if its momentum and charge are known. In the CAPRICE calorimeter the energy lost due to ionization is measured by each of the 16 silicon detectors traversed by a particle. To exploit this property, a variable QTOT was defined that corresponded to the total detected energy in all strips and at all planes. A particle was accepted as a muon if QTOT/$|$rig$|<60$. Figure 11(a) shows the total detected energy lost in the calorimeter divided by the rigidity of particles, which were selected as muons by the RICH and time-of-flight information from the ground data. The figure comprises 27903 events. The solid line at 60 indicates the chosen upper limit used to select muons. There are 27590 events below the limit and only 313 above. On the other hand, Fig. 11(b) shows the same plot but with electrons selected by the RICH from the float data. It is possible to see only 50 events below and 1047 above the solid line at 60. Therefore, it is clear that the calorimeter was efficient in selecting muons and rejecting electrons.

Figures 12 and 13 show a summary of the selection methods for positive and negative muons, respectively.

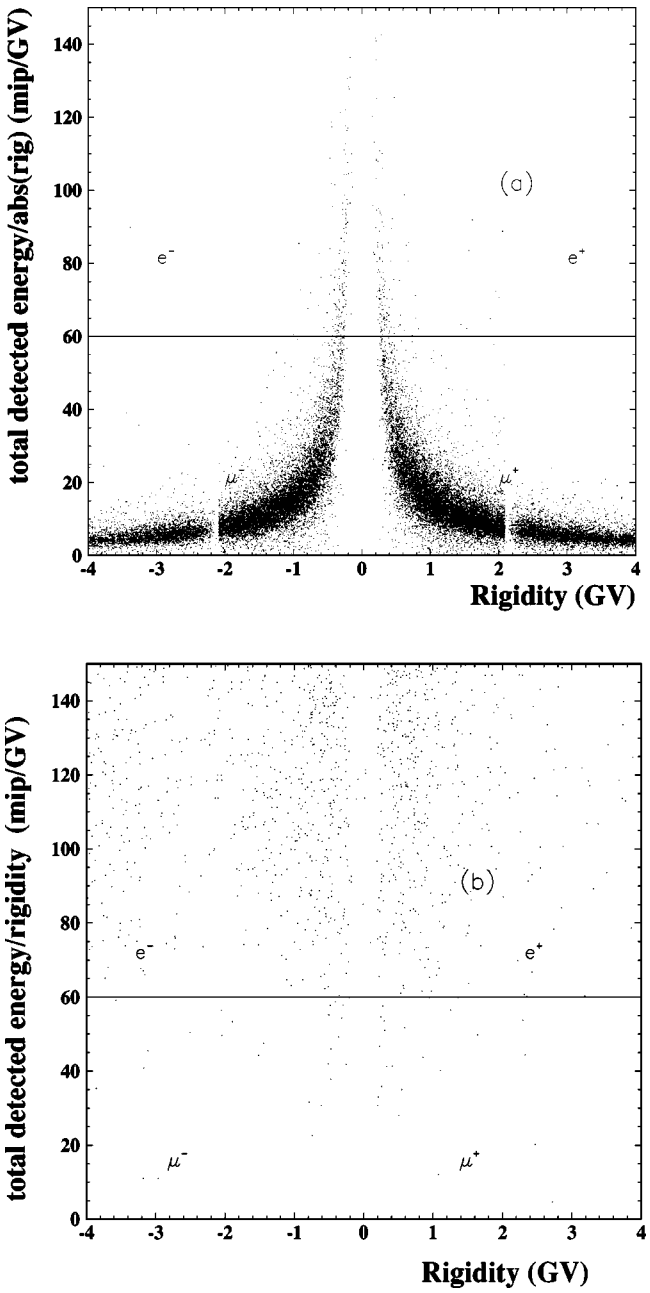

FIG. 11. Total energy loss in the calorimeter divided by the rigidity for (a) muons selected by the RICH and TOF detectors from the ground data (27903 events); (b) electrons selected by the RICH detector from the float data (1097 events). The solid line at 60 indicates the chosen upper limit used to select muons.

B. Contamination

We estimated the contamination of protons in the muon sample using the data at float, because it was easy to select a clean and large sample of protons. Below 1.5 GeV/c the TOF system was efficient in rejecting protons and the RICH system started to reject them at about 2.1 GeV/c. The overall proton rejection factor was better than 10^3 and hence, for ground and ascent data, the proton contamination was essentially negligible in all momentum intervals considered in this analysis, except between 1.5 and 2.1 GeV/c. In this interval

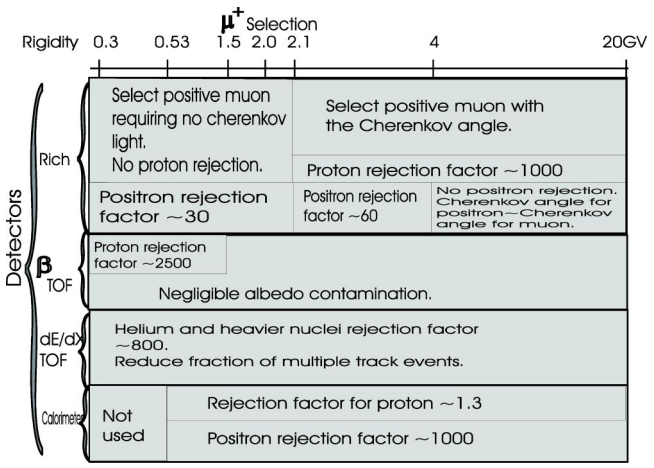

FIG. 12. Criteria used to select positive muons.

μ^+ could not be safely separated from protons and hence no results on μ^+ are presented for this momentum interval. For the float data a small contamination of protons was found and was subtracted. Electrons were efficiently rejected by the calorimeter above 0.53 GeV/c and by the RICH detector below about 5 GeV/c; hence the remaining electron contamination was negligible.

In the case of pion contamination, there were two types that could affect our data, namely, those which were produced in the gondola and those produced in the overlying atmosphere. In the first case, pions were produced by the interaction of protons in the gondola and for most momenta the pions looked like muons in the RICH detector. This contamination was significantly smaller in the case of CAPRICE94 since the RICH multiwire proportional chamber covered all the acceptance (in contrast to about 50% for CAPRICE98), and hence the RICH detector was more efficient in rejecting multiple-particle events. It is important to stress that these contaminations were more abundant below 1 GeV/c, because high energy pions are produced in interactions in which the kinematics is unfavorable to have just that particle alone traverse the apparatus without being accompanied by other charged particles. In the second case, only high energy pions (above about 10 GeV) have a small probability of reaching the gondola before decaying into muons in the atmosphere (e.g., see [28]).

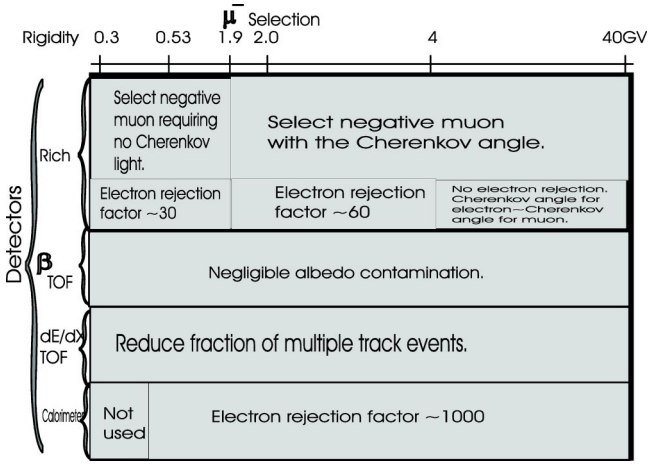

FIG. 13. Criteria used to select negative muons.

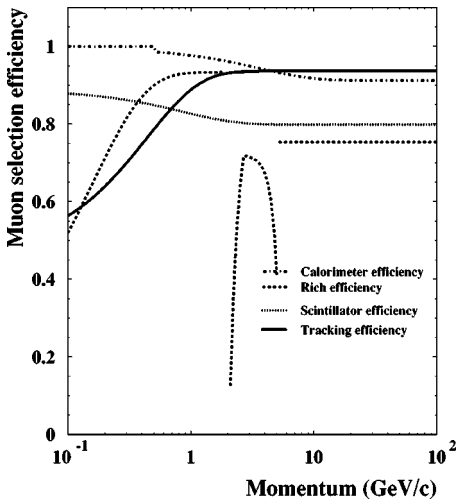

FIG. 14. Selection efficiencies as functions of rigidity for the data at ground.

To estimate the contamination of pions we selected interacting hadrons in the calorimeter and by a simulation calculated the efficiency and contamination of this selection. A simulation was used because it was not possible to select a clean sample of pions with the other detectors except for a small interval of rigidity with the RICH. However, the data in this small interval were very useful for checking the correctness of the result obtained with the simulation. Thus, by selecting interacting pions with the calorimeter and knowing the efficiency of this selection, it was possible to determine the pion contamination in the muon sample. However, because of the uncertainties in this procedure we decided not to present results on muons for momentum intervals in which the estimated contamination exceeded 20% of the muon sample. The background due to deuterons was very similar to

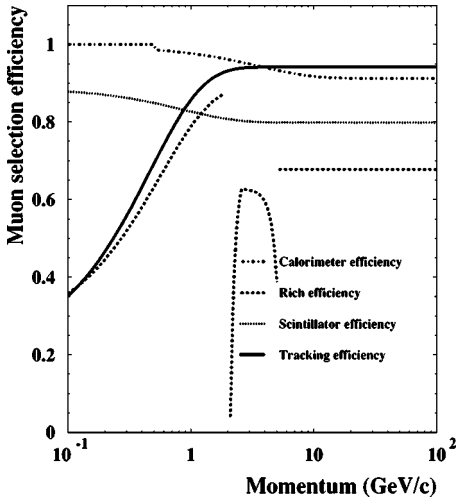

FIG. 15. Selection efficiencies as functions of rigidity for the data during ascent.

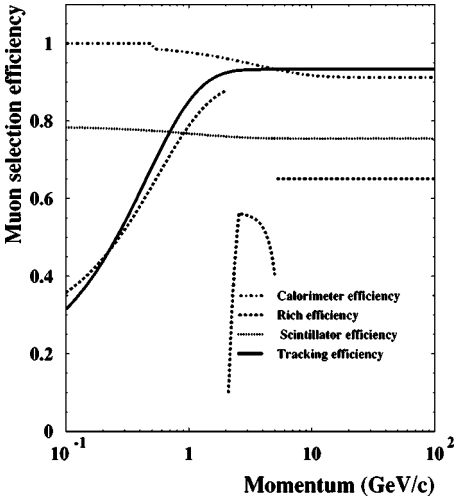

FIG. 16. Selection efficiencies as functions of rigidity for the data at float.

that of protons. Helium and heavier nuclei were efficiently rejected by the dE/dx selection.

C. Efficiency determination

In order to accurately determine the fluxes of the various types of particles, the efficiency of each detector was carefully studied using ground, ascent, and flight data. To determine the efficiency of a given detector, a data set of muons was selected by the remaining detectors. The number of muons correctly identified by the detector under test divided by the number of events in the data set is the efficiency. This procedure was repeated for each detector for a number of discrete rigidity bins. Using these, the efficiency of each detector was parametrized to allow an interpolation among bins. This parametrization could introduce systematic uncertainties on the total efficiency since the parameters were correlated. Thus, the error on the final efficiency was obtained using the error matrix of the fit for each detector.

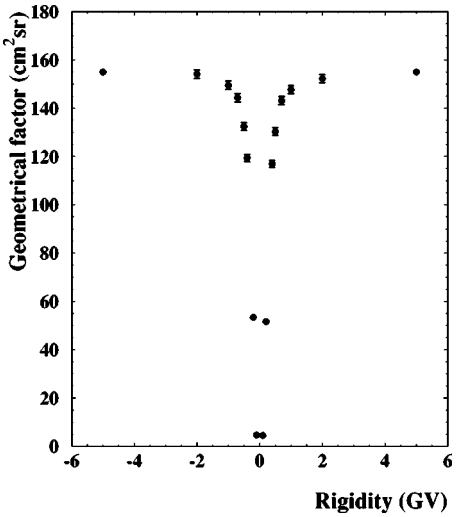

FIG. 17. Geometrical factor.

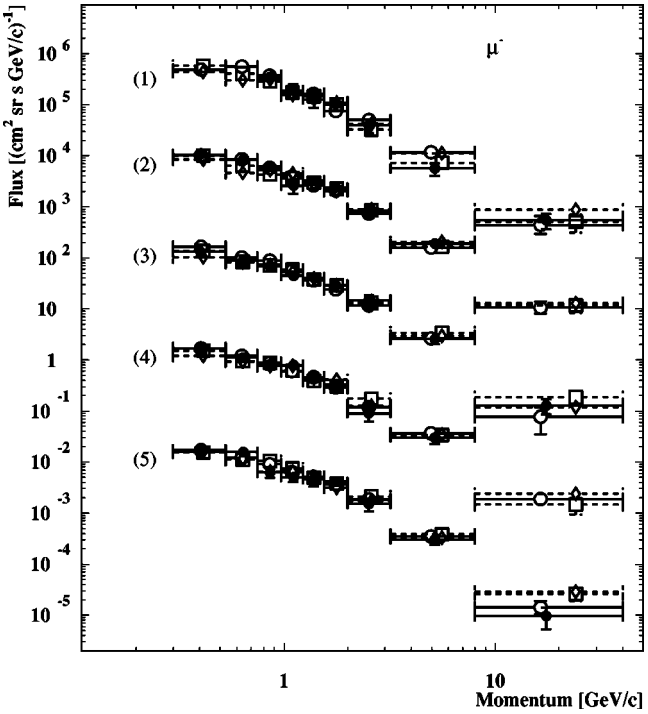

FIG. 18. Negative spectra for five atmospheric depth intervals in g/cm^2: (1) 15–33 g/cm^2, scaled by 10^8. (2) 33–65 g/cm^2, scaled by 10^6. (3) 65–90 g/cm^2, scaled by 10^4. (4) 90–120 g/cm^2, scaled by 10^2. (5) 120–150 g/cm^2, scaled by 1. ● CAPRICE98, ○ CAPRICE94, □ MASS89, and ◇ MASS91.

The efficiencies as functions of rigidity for different detectors are shown in Figs. 14, 15, and 16 for the ground, ascent, and float data, respectively.

1. RICH efficiency

It is important to note that the pressure in the RICH detector changed slightly during the flight. This implied a

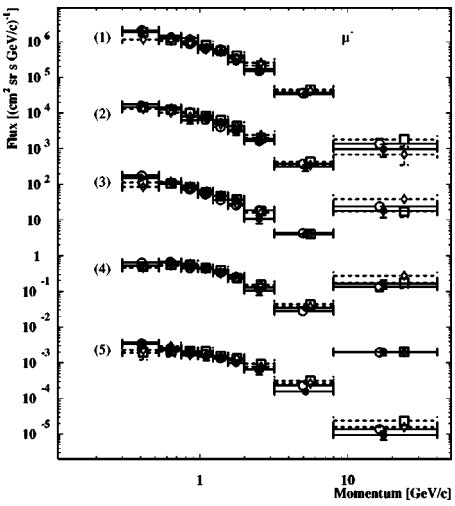

FIG. 19. Negative spectra for five atmospheric depth intervals in g/cm^2: (1) 150–190 g/cm^2, scaled by 10^8. (2) 190–250 g/cm^2, scaled by 10^6. (3) 250–380 g/cm^2, scaled by 10^4. (4) 380–581 g/cm^2, scaled by 10^2. (5) 581–885 g/cm^2, scaled by 1. ● CAPRICE98, ○ CAPRICE94, □ MASS89 and ◇ MASS91.

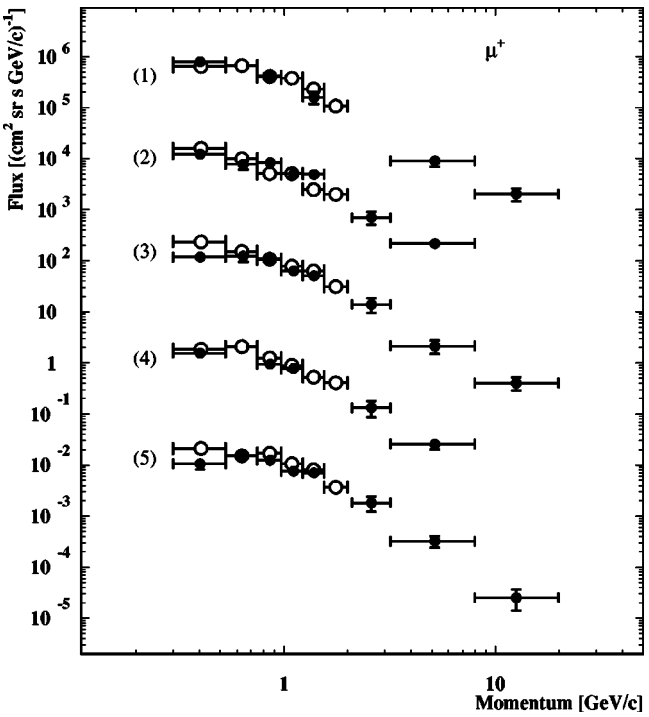

FIG. 20. Positive spectra for five atmospheric depth intervals in g/cm^2: (1) 15–33 g/cm^2, scaled by 10^8. (2) 33–65 g/cm^2, scaled by 10^6. (3) 65–90 g/cm^2, scaled by 10^4. (4) 90–120 g/cm^2, scaled by 10^2. (5) 120–150 g/cm^2, scaled by 1. ● CAPRICE98 and ○ CAPRICE94.

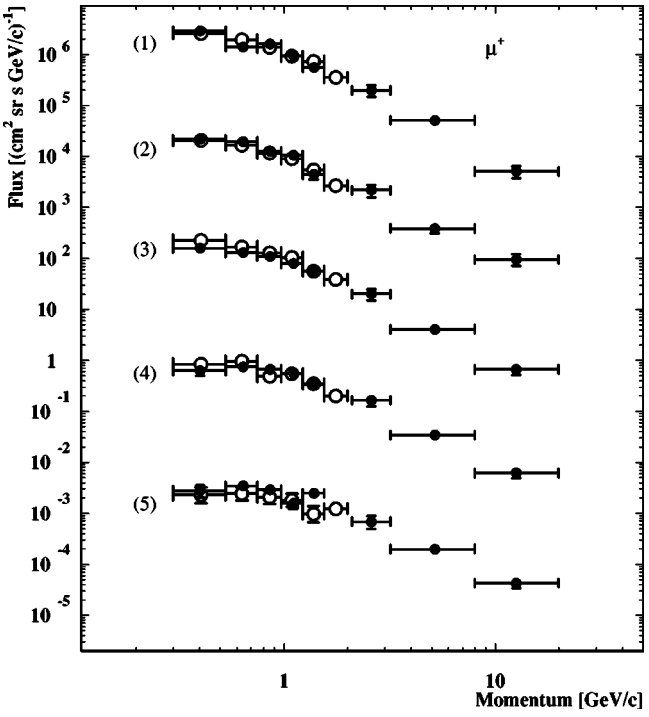

FIG. 21. Positive spectra for five atmospheric depth intervals in g/cm^2: (1) 150–190 g/cm^2, scaled by 10^8. (2) 190–250 g/cm^2, scaled by 10^6. (3) 250–380 g/cm^2, scaled by 10^4. (4) 380–581 g/cm^2, scaled by 10^2. (5) 581–885 g/cm^2, scaled by 1. ● CAPRICE98 and ○ CAPRICE94.

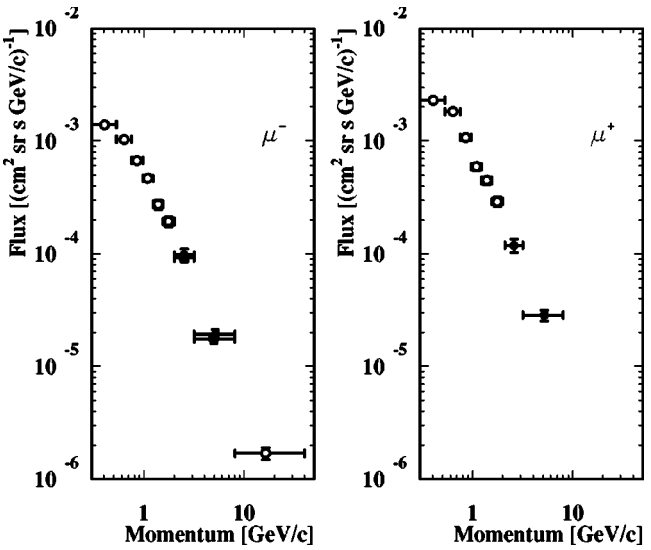

FIG. 22. The μ^+ and μ^- fluxes measured in the depth interval 5.45–5.95 g/cm^2 as a function of momentum. (●) CAPRICE98 data and (○) CAPRICE94 data.

variation in the refractive index and, consequently, in the number of photo-electrons produced, which resulted in a variation of the selection efficiency during the ascent and at float. However, at float and during ascent a large background of multiply charged particle events did not permit us to select a clean sample of muons, and hence the efficiency was estimated from ground data and scaled to the flight conditions. The scaling factor was obtained by comparing the number of photoelectrons produced at ground with that during the ascent and at float by selecting a clean sample of electrons (i.e., $\beta \simeq 1$ particles) using the calorimeter.

The muon selection efficiency as a function of momentum for ground, ascent, and float data is shown in Figs. 14, 15, and 16, respectively by dashed lines. Because of multiple scattering, the correlation between the particle impact posi-

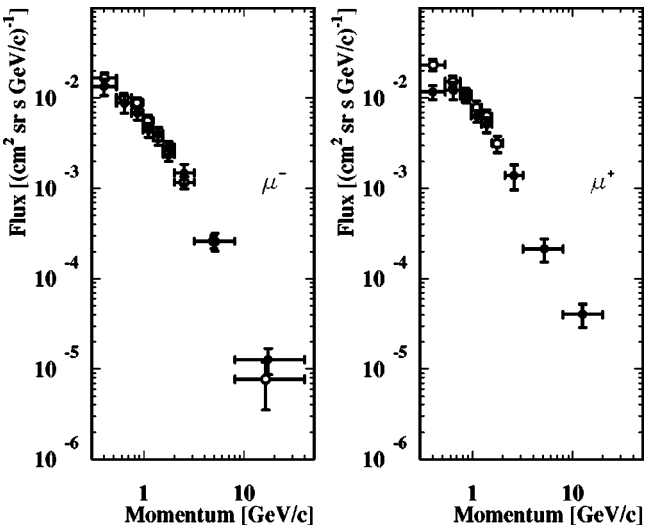

FIG. 23. The μ^+ and μ^- fluxes measured in the depth interval 65–90 g/cm^2 as a function of momentum. (●) CAPRICE98 data and (○) CAPRICE94 data.

TABLE I. The μ^+ and μ^- fluxes at ground altitude (885 g/cm^2). Column 1 is the momentum bin in the spectrometer. Columns 2 and 3 give the resulting μ^+ and μ^- fluxes. The errors include both statistical and efficiency-related systematic errors.

Momentum interval (GeV/c)	Flux (GeV/c cm^{2}sr s)$^{-1}$ μ^-	Flux (GeV/c cm^{2}sr s)$^{-1}$ μ^+
0.2–0.3	$(1.07\pm0.11)\times10^{-3}$	$(9.65\pm1.04)\times10^{-4}$
0.3–0.4	$(1.46\pm0.09)\times10^{-3}$	$(1.67\pm0.10)\times10^{-3}$
0.4–0.55	$(1.62\pm0.07)\times10^{-3}$	$(1.85\pm0.07)\times10^{-3}$
0.55–0.7	$(1.70\pm0.06)\times10^{-3}$	$(2.10\pm0.07)\times10^{-3}$
0.7–0.85	$(1.62\pm0.05)\times10^{-3}$	$(1.92\pm0.06)\times10^{-3}$
0.85–1.0	$(1.55\pm0.05)\times10^{-3}$	$(1.81\pm0.06)\times10^{-3}$
1.0–1.2	$(1.45\pm0.04)\times10^{-3}$	$(1.69\pm0.05)\times10^{-3}$
1.2–1.4	$(1.20\pm0.04)\times10^{-3}$	$(1.48\pm0.04)\times10^{-3}$
1.4–1.6	$(1.10\pm0.04)\times10^{-3}$	$(1.25\pm0.04)\times10^{-3}$
1.6–2.1	$(9.16\pm0.23)\times10^{-4}$	—
2.1–2.94	$(6.05\pm1.00)\times10^{-4}$	$(7.92\pm1.31)\times10^{-4}$
2.94–4.12	$(3.81\pm0.11)\times10^{-4}$	$(5.06\pm0.13)\times10^{-4}$
4.12–5.5	$(2.38\pm0.10)\times10^{-4}$	$(3.00\pm0.11)\times10^{-4}$
5.5–7.0	$(1.38\pm0.05)\times10^{-4}$	$(1.80\pm0.06)\times10^{-4}$
7.0–10.0	$(7.73\pm0.31)\times10^{-5}$	$(9.59\pm0.36)\times10^{-5}$
10.0–15.5	$(3.30\pm0.16)\times10^{-5}$	$(4.26\pm0.19)\times10^{-5}$
15.5–23.0	$(1.19\pm0.08)\times10^{-5}$	$(1.62\pm0.09)\times10^{-5}$
23.0–31.1	$(5.55\pm0.46)\times10^{-6}$	$(6.00\pm0.48)\times10^{-6}$
31.1–43.6	$(2.61\pm0.25)\times10^{-6}$	$(2.71\pm0.25)\times10^{-6}$
43.6–61.1	$(8.42\pm1.13)\times10^{-7}$	$(1.21\pm0.14)\times10^{-6}$
61.1–85.6	$(3.41\pm0.6)\times10^{-7}$	$(3.81\pm0.63)\times10^{-7}$
85.6–120	$(1.50\pm0.33)\times10^{-7}$	$(1.29\pm0.31)\times10^{-7}$

tion in the RICH detector and the extrapolation from the tracker was decreasing with momenta below about 1 GeV/c, and consequently so was the selection efficiency. However, this condition was not used for the ground data, resulting in a higher selection efficiency, as can be seen from Fig. 14.

The efficiency drops to almost zero at $\sim$2 GeV/c where muons start to produce Cherenkov light, as they were selected requiring no light below $\sim$2 GeV/c. Above this momentum, the selection is done by Cherenkov angle reconstruction and the efficiency increases, reaching a constant value above 5 GeV/c. Between 3 and 5 GeV/c the efficiency decreases because of the additional selection condition used in this momentum range to reject pions.

2. TOF efficiency

The flight data were not free from some contamination from multiple charged particles produced by interactions of cosmic rays in the payload structure. Hence, the efficiency could not be estimated directly from these data. However, it was found that the performance of the TOF system concerning the energy loss selection did not vary from ground to float data. Thus, the efficiency of this condition was obtained from the more statistically significant ground data. In contrast, it was found that the efficiency of the β selection varied during the flight. However, by using the condition on the energy loss it was possible to select a clean sample of muons from flight data, and hence we could determine the efficiency of the β selection directly for the flight data. So the final TOF efficiency for the data during ascent and at float were given by the product of (1) dE/dx efficiency, obtained from ground data, and (2) β selection efficiency using flight data.

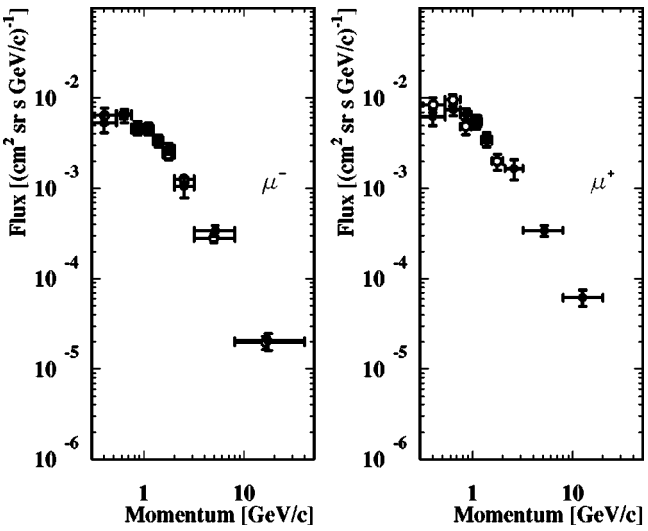

FIG. 24. The $\mu^+$and μ^- fluxes at the depth interval 380–581 g/cm^2 as a function of momentum. (●) CAPRICE98 data and (○) CAPRICE94 data.

3. Calorimeter efficiency

The calorimeter was not used below 0.53 GeV/c. At higher momenta the efficiency was obtained using ground data. This was cross-checked with flight data, in which contamination of interacting particles was present. A good agreement was found between these two efficiencies within the uncertainties, and hence the calorimeter efficiency obtained from the ground data was used also for the flight data.

4. Tracking efficiency

The determination of the tracking efficiency is, usually, the most demanding to perform. This efficiency, in fact, depends on the momenta of the particles, and these momenta need to be obtained independently of the tracking system.

Two methods were developed to determine the tracking efficiency. Both were based on codes that were independent of the drift chamber tracking system and, instead, used the other detectors available for this purpose. The first method, called the ''no-DC'' method, used the position information of the ionization cluster in the MWPC of the RICH detector, the two time-of-flight scintillation detectors (only in the x direction), and the electromagnetic calorimeter to reconstruct the track of the particle traversing the detector system. The second method, called the ''RICH'' method, used the RICH detector to get the rigidity from the velocity (β) derived from the Cherenkov angle measurement with the help of an extrapolated straight track from the calorimeter (see [29]). In Figs. 14, 15, and 16 (solid line) it is possible to see the efficiency at ground, ascent and float, respectively. In all

TABLE II. Measured atmospheric growth fluxes [in units of particles/(GeV/c cm^2)] for negative muons in the 0.3 −40 GeV/c momentum range. Results are given for the following momentum intervals: (I) 0.3–0.53 GeV/c, (II) 0.53–0.75 GeV/c, (III) 0.75–0.97 GeV/c, (IV) 0.97–1.23 GeV/c, (V) 1.23–1.55 GeV/c, (VI) 1.55–2.0 GeV/c, (VII) 2.0–3.2 GeV/c, (VIII) 3.2–8 GeV/c, and (IX) 8–40 GeV/c. The errors include both statistical and efficiency-related systematic errors.

Initial depth (g/cm^2)	885	581	380
Final depth (g/cm^2)	581	380	250
Average depth (g/cm^2)	704	462	308
I μ^- Flux	$(3.67\pm0.84)\times10^{-3}$	$(5.34\pm1.19)\times10^{-3}$	$(1.52\pm0.24)\times10^{-2}$
II μ^- Flux	$(2.24\pm0.52)\times10^{-3}$	$(6.38\pm1.04)\times10^{-3}$	$(1.11\pm0.16)\times10^{-2}$
III μ^- Flux	$(2.09\pm0.45)\times10^{-3}$	$(4.74\pm0.80)\times10^{-3}$	$(9.28\pm1.30)\times10^{-3}$
IV μ^- Flux	$(1.49\pm0.33)\times10^{-3}$	$(4.62\pm0.68)\times10^{-3}$	$(6.79\pm0.96)\times10^{-3}$
V μ^- Flux	$(1.44\pm0.28)\times10^{-3}$	$(3.39\pm0.50)\times10^{-3}$	$(4.7\pm0.69)\times10^{-3}$
VI μ^- Flux	$(9.69\pm1.88)\times10^{-4}$	$(2.79\pm0.38)\times10^{-3}$	$(3.71\pm0.50)\times10^{-3}$
VII μ^- Flux	$(6.42\pm1.70)\times10^{-4}$	$(1.05\pm0.27)\times10^{-3}$	$(1.08\pm0.29)\times10^{-3}$
VIII μ^- Flux	$(1.55\pm0.28)\times10^{-4}$	$(3.42\pm0.48)\times10^{-4}$	$(4.00\pm0.61)\times10^{-4}$
IX μ^- Flux	$(9.38\pm2.53)\times10^{-6}$	$(2.04\pm0.44)\times10^{-5}$	$(1.64\pm0.46)\times10^{-5}$
250	190	150	120
190	150	120	90
219	165	136	104
$(1.78\pm0.34)\times10^{-2}$	$(1.84\pm0.28)\times10^{-2}$	$(1.57\pm0.30)\times10^{-2}$	$(1.69\pm0.34)\times10^{-2}$
$(1.46\pm0.24)\times10^{-2}$	$(1.47\pm0.19)\times10^{-2}$	$(1.58\pm0.24)\times10^{-2}$	$(1.10\pm0.18)\times10^{-2}$
$(6.36\pm1.43)\times10^{-3}$	$(1.28\pm1.61)\times10^{-2}$	$(6.24\pm1.31)\times10^{-3}$	$(8.29\pm1.83)\times10^{-3}$
$(8.31\pm1.41)\times10^{-3}$	$(7.11\pm1.03)\times10^{-3}$	$(5.06\pm1.02)\times10^{-3}$	$(8.02\pm1.19)\times10^{-3}$
$(5.71\pm1.01)\times10^{-3}$	$(4.90\pm0.74)\times10^{-3}$	$(4.61\pm1.26)\times10^{-3}$	$(4.58\pm0.78)\times10^{-3}$
$(3.01\pm0.60)\times10^{-3}$	$(2.72\pm0.45)\times10^{-3}$	$(4.10\pm0.65)\times10^{-3}$	$(3.28\pm0.66)\times10^{-3}$
$(1.84\pm0.51)\times10^{-3}$	$(1.74\pm0.43)\times10^{-3}$	$(1.51\pm0.42)\times10^{-3}$	$(9.02\pm2.81)\times10^{-4}$
$(3.08\pm0.71)\times10^{-4}$	$(3.37\pm0.58)\times10^{-4}$	$(3.04\pm0.65)\times10^{-4}$	$(3.00\pm0.71)\times10^{-4}$
$(1.80\pm0.64)\times10^{-5}$	$(9.61\pm3.64)\times10^{-6}$	$(9.57\pm4.29)\times10^{-6}$	—
90	65	33	5.95
65	33	15	5.45
77	48.4	22.6	5.5
$(1.34\pm0.27)\times10^{-2}$	$(1.06\pm0.16)\times10^{-2}$	—	—
$(8.78\pm2.01)\times10^{-3}$	$(8.40\pm1.41)\times10^{-3}$	—	—
$(6.85\pm1.12)\times10^{-3}$	$(6.29\pm0.85)\times10^{-3}$	$(3.50\pm0.55)\times10^{-3}$	—
$(4.44\pm0.78)\times10^{-3}$	$(2.60\pm0.79)\times10^{-3}$	$(1.91\pm0.60)\times10^{-3}$	—
$(4.04\pm0.64)\times10^{-3}$	$(3.29\pm0.60)\times10^{-3}$	$(1.26\pm0.39)\times10^{-3}$	—
$(2.86\pm0.44)\times10^{-3}$	$(2.38\pm0.32)\times10^{-3}$	$(1.03\pm0.18)\times10^{-3}$	—
$(1.48\pm0.37)\times10^{-3}$	$(8.41\pm2.17)\times10^{-4}$	$(3.92\pm1.16)\times10^{-4}$	$(9.75\pm1.32)\times10^{-5}$
$(2.59\pm0.57)\times10^{-4}$	$(1.89\pm0.33)\times10^{-4}$	$(5.65\pm1.57)\times10^{-5}$	$(1.93\pm0.19)\times10^{-5}$
$(1.27\pm0.40)\times10^{-5}$	—	$(5.42\pm1.82)\times10^{-6}$	—

three cases the two methods gave consistent results. The efficiency decreases for low rigidities and it reaches a plateau of constant efficiency at $\simeq$94% above $\simeq$2.5 GV.

IV. THE FLUX

A. Efficiency correction

The rigidity range was split into bins with small enough widths to assure negligible variation of efficiencies in each bin. The mean efficiency ($\overline{\varepsilon}$) was obtained with a weighting technique:

$$\overline{\varepsilon} = \frac{\int \epsilon(E) J(E) dE}{\int J(E) dE},$$

where $J(E)$ is the flux of particles. The flux of atmospheric muons at ground measured by the CAPRICE97 experiment [16] was used.

TABLE III. Measured atmospheric growth fluxes [in units of particles/ (GeV/c cm^2)] for positive muons in the 0.3–20 GeV/c momentum range. Results are given for the following momentum intervals: (I) 0.3–0.53 GeV/c, (II) 0.53–0.75 GeV/c, (III) 0.75–0.97 GeV/c, (IV) 0.97–1.23 GeV/c, (V) 1.23–1.55 GeV/c, (VI) 1.55–2.1 GeV/c, (VII) 2.1–3.2 GeV/c, (VIII) 3.2–8 GeV/c, and (IX) 8–20 GeV/c. The errors include both statistical and efficiency-related systematic errors.

Initial depth (g/cm^2)	885	581	380
Final depth (g/cm^2)	581	380	250
Average depth (g/cm^2)	704	462	308
I μ^+ Flux	$(2.81\pm0.74)\times10^{-3}$	$(6.20\pm1.31)\times10^{-3}$	$(1.58\pm0.25)\times10^{-2}$
II μ^+ Flux	$(3.46\pm0.65)\times10^{-3}$	$(7.44\pm1.13)\times10^{-3}$	$(1.30\pm0.17)\times10^{-2}$
III μ^+ Flux	$(2.88\pm0.53)\times10^{-3}$	$(6.65\pm0.95)\times10^{-3}$	$(1.10\pm0.14)\times10^{-2}$
IV μ^+ Flux	$(1.58\pm0.34)\times10^{-3}$	$(5.57\pm0.75)\times10^{-3}$	$(7.93\pm1.05)\times10^{-3}$
V μ^+ Flux	$(2.47\pm0.37)\times10^{-3}$	$(3.42\pm0.51)\times10^{-3}$	$(5.73\pm0.77)\times10^{-3}$
VI μ^+ Flux	—	—	—
VII μ^+ Flux	$(6.83\pm1.89)\times10^{-4}$	$(1.66\pm0.41)\times10^{-3}$	$(2.01\pm0.51)\times10^{-3}$
VIII μ^+ Flux	$(1.98\pm0.31)\times10^{-4}$	$(3.42\pm0.48)\times10^{-4}$	$(4.08\pm0.62)\times10^{-4}$
IX μ^+ Flux	$(4.28\pm0.89)\times10^{-5}$	$(6.19\pm1.25)\times10^{-5}$	$(6.71\pm1.51)\times10^{-5}$
250	190	150	120
190	150	120	90
219	165	136	104
$(2.20\pm0.39)\times10^{-2}$	$(2.88\pm0.36)\times10^{-2}$	$(1.07\pm0.24)\times10^{-2}$	$(1.56\pm0.30)\times10^{-2}$
$(1.96\pm0.29)\times10^{-2}$	$(1.42\pm0.19)\times10^{-2}$	$(1.50\pm0.23)\times10^{-2}$	—
$(1.25\pm0.20)\times10^{-2}$	$(1.61\pm0.18)\times10^{-2}$	$(1.25\pm0.23)\times10^{-2}$	$(9.43\pm1.51)\times10^{-3}$
$(1.05\pm0.16)\times10^{-2}$	$(9.51\pm1.20)\times10^{-3}$	$(7.53\pm1.26)\times10^{-3}$	$(7.72\pm1.18)\times10^{-3}$
$(4.44\pm0.91)\times10^{-3}$	$(5.53\pm0.80)\times10^{-3}$	$(6.97\pm1.05)\times10^{-3}$	—
—	—	—	—
$(2.20\pm0.62)\times10^{-3}$	$(1.99\pm0.51)\times10^{-3}$	$(1.82\pm0.59)\times10^{-3}$	$(1.32\pm0.46)\times10^{-3}$
$(3.87\pm0.80)\times10^{-4}$	$(5.13\pm0.72)\times10^{-4}$	$(3.20\pm0.80)\times10^{-4}$	$(2.59\pm0.56)\times10^{-4}$
$(9.57\pm2.41)\times10^{-5}$	$(5.11\pm1.38)\times10^{-5}$	$(2.53\pm1.14)\times10^{-5}$	—
90	65	33	5.95
65	33	15	5.45
77	48.4	22.6	5.5
$(1.17\pm0.21)\times10^{-2}$	$(1.21\pm0.19)\times10^{-2}$	$(7.95\pm1.52)\times10^{-3}$	—
$(1.22\pm0.26)\times10^{-2}$	$(7.75\pm1.61)\times10^{-3}$	—	—
$(1.10\pm0.17)\times10^{-2}$	$(8.39\pm1.00)\times10^{-3}$	$(4.23\pm0.86)\times10^{-3}$	—
$(6.35\pm0.94)\times10^{-3}$	$(5.05\pm0.67)\times10^{-3}$	—	—
$(5.12\pm1.00)\times10^{-3}$	$(4.96\pm0.57)\times10^{-3}$	$(1.60\pm0.43)\times10^{-3}$	—
—	—	—	—
$(1.39\pm0.43)\times10^{-3}$	$(7.07\pm2.04)\times10^{-4}$	—	$(1.19\pm0.16)\times10^{-4}$
$(2.13\pm0.61)\times10^{-4}$	$(2.19\pm0.36)\times10^{-4}$	$(9.10\pm2.05)\times10^{-5}$	$(2.86\pm^{0.34}_{0.29})\times10^{-5}$
$(4.04\pm1.18)\times10^{-5}$	—	$(2.04\pm0.58)\times10^{-5}$	—

B. Energy loss corrections

When particles traverse the gondola and the detectors down to the level of the spectrometer, they lose energy due to ionization. The width of the momentum bin was corrected for these ionization losses.

C. Dead time and geometrical factor

The live time (T_{live}) was calculated by multiplying the effective exposure time by the fractional live time. The fractional live time was given by two scalers in the payload: one continually running and the other running only when the data acquisition system was not busy. The ratio between these two scalers is the fractional live time of the experiment. For the muons in the atmosphere, the fractional live time was calculated for every interval of time during the ascent of the balloon (the intervals of time are related to the altitude).

The geometrical factor was obtained with Monte Carlo techniques [30]; the simulation implemented the same track-fitting algorithm used in the analysis to trace particles through the spectrometer. The resulting geometrical factor is presented in Fig. 17.

D. Calculating the flux

The values of the μ^+ and μ^- fluxes ($J_{spe}^{\mu^+,\mu^-}$) were obtained according to

$$J_{spe}^{\mu^+,\mu^-}(P)=\frac{1}{T_{live}\times G^{\mu^+,\mu^-}(P)\times\Delta P}\times N_{spe}^{\mu^+,\mu^-}(P), \tag{2}$$

where P is the momentum, T_{live} is the live time, $G^{\mu^+,\mu^-}(P)$ are the geometrical factors, ΔP is the width of the momentum bin corrected for ionization losses to the top of the payload, and $N_{spe.}^{\mu^+,\mu^-}(P)$ is the total number of μ^+ and μ^- in the spectrometer obtained taking into account all the selection efficiencies.

E. Systematic uncertainties

Systematic uncertainties originating from the determination of the detector efficiencies, discussed in Sec. III C, were included in the errors given in tables and shown in figures.

Another possible systematic error was related to the efficiency of the trigger system. This was studied prior to the launch with a system providing particle coincidence between two scintillators, one placed above and the other below the TOF system. The efficiency was found to be close to 100% with an uncertainty of about 2%. The performance of each photomultiplier pair was also tested by comparing the spatial distribution of triggers during the flight with the distribution from the same simulation used for the geometrical factor, and an excellent agreement was found.

The method for calculating the geometrical factor used in this work was compared with two other techniques in the CAPRICE94 analysis, and it was found to be in agreement within 2% above 0.5 GV. Considering the similar geometrical configuration of CAPRICE98, it can be concluded that the uncertainty in the geometrical factor was about 2%.

There was also an uncertainty in the measurement of the atmospheric depth. For the float data a residual atmospheric depth of 5.5 g/cm^2 was given by a pressure sensor owned and calibrated by the CAPRICE98 collaboration. The pressure was also measured by a detector owned and calibrated by the National Scientific Balloon Facility (NSBF). The NSBF pressure data were about 15% lower at float than the ones measured by our sensor. We interpreted this difference as the systematic uncertainty in the measured depth (all atmospheric depths presented in this paper were derived using our pressure data). However, this uncertainty does not affect the results but has to be taken into account when comparing the measured spectra with the simulated ones.

Systematic uncertainties related to the tracking system are discussed in detail in [9].

V. RESULTS

The absolute particle fluxes were calculated using Eq. (2). The resulting muon fluxes at ground are presented in Table I and at several atmospheric depths and momenta interval in Tables II and III for negative and positive muons, respectively. Figures 18, 19, 20, and 21 show the flux as a function of momentum for positive and negative muons at different atmospheric depths. The data are compared with data from the CAPRICE94 experiment [11] and in the case of negative muons also with data from the MASS89 [12] and MASS91 [13] experiments. A good agreement is found for the μ^- data from the different experiments. Above 1 GeV/c the flux decreases smoothly with momentum p, approximately following an e^{-p/p_0} dependence with $p_0\approx 0.5$ GeV/c. The μ^+ data show good agreement between CAPRICE94 and CAPRICE98 data below 2 GeV/c. The new μ^+ above 2 GeV/c shows the same dependence on momentum as the μ^- data.

In Fig. 22 we compare the data at float 5.5 g/cm^2 with the corresponding CAPRICE94 data. Due to the pion contamination the CAPRICE98 results are limited to the range 2–8 GeV/c. There is good agreement in the region of overlap.

In Figs. 23 and 24 we present the muon spectra at two selected depths intervals, 65–90 g/cm^2 and 380 $-$581 g/cm^2. Below about 1 GeV/c the CAPRICE98 results are lower than those of CAPRICE94, which might indicate geomagnetic effects. It is worth pointing out that for both CAPRICE98 and CAPRICE94 the solar modulation was close to the minimum.

Finally, it is important to stress that this measurement of the flux of muons is a powerful tool to check and/or calibrate air shower simulation programs. There is a new project discussed by the Wizard Collaboration to refly CAPRICE98, stopping at different atmospheric depths to sample the muon flux. This new experiment will improve the muon statistics and will allow a more detailed comparison of μ^+ and μ^- fluxes. It also will remove the problem of averaging the value of atmospheric depth of measurements, since the data will be collected at approximately fixed altitudes [31].

ACKNOWLEDGMENTS

This work was supported by NASA Grant No. NADW–110, the Istituto Nazionale di Fisica Nucleare, Italy, the Agenzia Spaziale Italiana, DARA and DFG in Germany, the Swedish National Space Board, and the Knut and Alice Wallenberg foundation. P.H. was supported by the Swedish Foundation for International Cooperation in Research and Higher Education; E.M. was supported by the Foundation BLANCEFLOR Boncompagni-Ludovisi, née Bildt. We wish to thank the National Scientific Balloon Facility and the NSBF launch crew that served in Fort Sumner. We would also like to acknowledge the essential support given by the Gas Work Group (EST/SM/SF) and the Thin Film and Glass Laboratory (EP-TA1-SD) at CERN, the LEPSI and CRN Strasbourg, and the technical staff of NMSU and of INFN.

[1] Y. Fukuda *et al.*, Phys. Rev. Lett. **81**, 1562 (1998).
[2] W. W. M. Allison *et al.*, Phys. Lett. B **391**, 491 (1997); *ibid.* **449**, 137 (1999).
[3] M. Ambrosio *et al.*, Phys. Lett. B **434**, 451 (1998).
[4] T. Gaisser, hep-ph/0209195.
[5] P. Carlson, P. Hansen, and S. Sciutto, ''Flux of Atmospheric Muons: Comparison between AIRES Simulation and CAPRICE98 Data'' (in preparation).
[6] S. J. Sciutto, in *Proceedings of the 27th International Cosmic Ray Conference*, Hamburg (Schaltungsdienst Lange, Berlin, 2001), Vol. 1, p. 237.
[7] T. K. Gaisser *et al.*, Phys. Rev. D **54**, 5578 (1996); see also Nucl. Phys. B (Proc. Suppl.) **77**, 133 (1999); M. Honda, *ibid.* **77**, 140 (1999).
[8] T. Gaisser and M. Honda, hep-ph/0203272.
[9] M. Boezio *et al.*, Astropart. Phys. (to be published), astro-ph/0212253.
[10] G. Barr *et al.*, in *Proceedings of the 27th International Cosmic Ray Conference*, Hamburg [6], Vol. 1, p. 1585.
[11] M. Boezio *et al.*, Phys. Rev. Lett. **82**, 4757 (1999); Phys. Rev. D **62**, 032007 (2000).
[12] R. Bellotti *et al.*, Phys. Rev. D **53**, 35 (1996).
[13] R. Bellotti *et al.*, Phys. Rev. D **60**, 052002 (1999).
[14] S. Coutu *et al.*, Phys. Rev. D **62**, 032001 (2000).
[15] T. Sanuki *et al.*, Phys. Lett. B **541**, 234 (2002).
[16] J. Kremer *et al.*, Phys. Rev. Lett. **83**, 4241 (1999).
[17] M. L. Ambriola *et al.*, Nucl. Phys. **B78**, 32 (1999).
[18] M. Boezio *et al.*, Adv. Space Res. **27**, 669 (2001).
[19] M. Circella *et al.*, Adv. Space Res. **27**, 755 (2001).
[20] M. Boezio *et al.*, Astrophys. J. **56**, 787 (2001); D. Bergström *et al.*, Astrophys. J. Lett. **534**, L177 (2000).
[21] P. Carlson *et al.*, Nucl. Instrum. Methods Phys. Res. A **349**, 577 (1994); G. Barbiellini *et al.*, *ibid.* **371**, 169 (1996).
[22] T. Francke *et al.*, Nucl. Instrum. Methods Phys. Res. A **433**, 87 (1999).
[23] D. Bergström *et al.*, Nucl. Instrum. Methods Phys. Res. A **463**, 161 (2001).
[24] D. Bergström, Licentiat Thesis, Royal Institute of Technology, Stockholm, 2000, available electronically at http://www.particle.kth.se/group_docs/admin/theses.html#lic
[25] R. L. Golden *et al.*, Nucl. Instrum. Methods **148**, 179 (1978).
[26] M. Hof *et al.*, Nucl. Instrum. Methods Phys. Res. A **345**, 561 (1994).
[27] M. Bocciolini *et al.*, Nucl. Instrum. Methods Phys. Res. A **370**, 403 (1996); *ibid.* **333**, 77 (1993); M. Ricci *et al.*, in *Proceedings of the 26th International Cosmic Ray Conference*, Salt Lake City (University of Utah Press, Salt Lake City, 1999), Vol. 5, p. 49.
[28] G. D. Badhwar, S. A. Stephens, and R. L. Golden, Phys. Rev. D **15**, 820 (1977).
[29] D. Bergström, Ph.D. Thesis, Royal Institute of Technology, Stockholm, 2001, available at http://www.particle.kth.se/group_docs/admin/theses.html#phd
[30] J. D. Sullivan, Nucl. Instrum. Methods **95**, 5 (1971).
[31] M. Circella *et al.*, in *Proceedings of the 27th International Cosmic Ray Conference*, Hamburg [6], Vol. 1, p. 1251.